



# High purity single photons entangled with an atomic qubit

C. CROCKER,\* M. LICHTMAN, K. SOSNOVA, A. CARTER, S. SCARANO, AND C. MONROE 

*Joint Quantum Institute, Center for Quantum Information and Computer Science, and Department of Physics, University of Maryland, College Park, MD 20742, USA*

\*ccrocker@umd.edu

**Abstract:** Trapped atomic ions are an ideal candidate for quantum network nodes, with long-lived identical qubit memories that can be locally entangled through their Coulomb interaction and remotely entangled through photonic channels. The integrity of this photonic interface is generally reliant on the purity of single photons produced by the quantum memory. Here, we demonstrate a single-photon source for quantum networking based on a trapped  $^{138}\text{Ba}^+$  ion with a single photon purity of  $g^{(2)}(0) = (8.1 \pm 2.3) \times 10^{-5}$  without background subtraction. We further optimize the tradeoff between the photonic generation rate and the memory-photon entanglement fidelity for the case of polarization photonic qubits by tailoring the spatial mode of the collected light.

© 2019 Optical Society of America under the terms of the [OSA Open Access Publishing Agreement](#)

## 1. Introduction

Entanglement between flying photonic qubits and local memory qubits is an essential component of quantum communication networks and distributed quantum computers [1–6]. Trapped atomic ions provide a natural way to generate this entanglement, with pure and replicable quantum memories that can be locally entangled through their mutual Coulomb interaction [7,8] and also emit nearly identical photons for networking. When photons are emitted from appropriate atomic excited states, the memory qubit can become entangled with the photonic qubit [9]. This entanglement is generally degraded if the atom is re-excited after a photon is emitted or background photons are present, thus the purity of the single-photon source is critical for high fidelity atom-photon entanglement [10]. Moreover, for non-zero collection solid angles, the atomic radiation pattern does not perfectly map onto experimental polarization modes, limiting free-space entanglement fidelity in the case of polarization qubits [11]. Here, we demonstrate methods for reducing these errors by using different colors of light for excitation and collection, and by applying a custom aperture to maximize collected light while keeping polarization mixing errors low.

The barium ion is an excellent candidate for trapped ion quantum network nodes [12–16]. While most ions have their primary transitions in the UV wavelengths, barium has two lines in the visible range: a primary cooling transition at 493 nm ( $6^2S_{1/2}$  to  $6^2P_{1/2}$ ) and an auxiliary transition at 650 nm ( $5^2D_{3/2}$  to  $6^2P_{1/2}$ ). Compared to the UV transitions in most ions, photons in these visible wavelengths suffer less attenuation through optical fibers, permit access to a wide range of supporting photonic technologies, and can be converted to IR wavelengths for longer-distance networks [17]. In this work we store the memory qubit in the two Zeeman levels of the  $^{138}\text{Ba}^+$   $6^2S_{1/2}$  ground state:  $|m_J = -1/2\rangle \equiv |\downarrow\rangle$  and  $|m_J = +1/2\rangle \equiv |\uparrow\rangle$ . To generate ion-photon entanglement, 493 nm photons are collected from decays from the  $6^2P_{1/2}$   $|J = 1/2, m_J = +1/2\rangle \equiv |e\rangle$  excited state (see Fig. 1(a)) based on excitation from the  $5^2D_{3/2}$   $|J = 3/2, m_J = +3/2\rangle$  state.

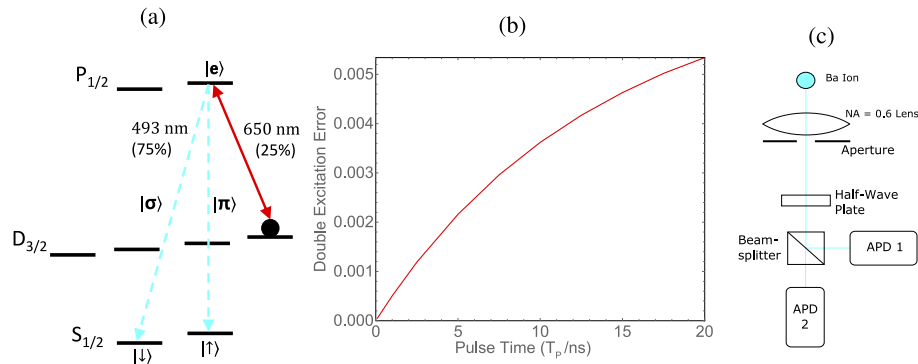


**Fig. 1.** (a) Energy level diagram for  $^{138}\text{Ba}^+$  atom including branching ratios from  $|e\rangle$  to the S and D manifolds. (b) Double excitation errors plotted as a function of pulse time  $T_p$  assuming a Rabi rate of  $\Omega = \pi/T_p$ . Note that even for pulses of order  $T_p \sim \tau_e = 10.5$  ns the double excitation error is low. This low error rate is important, as it cannot be reduced by spatial filtering. (c) Sketch of the setup used to collect light and analyze the polarization of photonic qubits. Light is collected by a NA = 0.6 objective located outside of the vacuum window and then directed through a half-wave plate that can perform x-rotations on the polarization qubit. Next is a polarizing, beam-splitting cube and a pair of APDs (Laser Components COUNT-10B) to detect the photon's polarization.

## 2. Double excitations

We first examine the effects of double excitations on the fidelity of ion-photon entanglement in this system. For probabilistic photon collection based on emission from an excited state  $|e\rangle$ , there are two mechanisms by which double excitations can introduce errors. In the first mechanism, the first photon emitted by the atom is collected, but the second photon is not. Here, the second excitation degrades the entanglement between the first photon and the state of the atom. In the second mechanism, the first photon is not collected but the second photon is. This situation still produces entanglement between the ion and the collected photon, but the scrambling of the atomic state after the first photon introduces errors into the fidelity of the desired entangled state.

Our previous work has shown ion-photon entanglement with  $^{138}\text{Ba}^+$  by first pumping into  $|\downarrow\rangle$  and exciting the atom to  $|e\rangle$  with continuous-wave (CW) light at 493 nm [18]. Because this scheme uses the same line for excitation and collection light, it is susceptible to both types of double-excitation errors. These can be mitigated with a fast pulse of excitation light of duration  $T_p \ll \tau_e$  where  $\tau_e$  is the excited state lifetime [19]. Alternatively, the atom can be weakly excited with probability  $P_e \ll 1$  such that the probability of double excitations scales as  $P_e^2$  [20]. However, weak excitation reduces the overall entanglement success rate and forces a fundamental tradeoff between entanglement generation rate and fidelity [21].

To avoid the difficulties caused by weak excitation and to eliminate the first mechanism of double excitation errors, we initialize the  $\text{Ba}^+$  ion in the  $5^2D_{3/2}$  manifold, excite with 650 nm light, and collect 493 nm fluorescence [17,22,23]. Barium's  $5^2D_{3/2}$  level features an 80 s lifetime [24], much longer than conceivable quantum operations, and its 3:1 branching ratio from the  $6^2P_{1/2}$  state provides fast initialization and excitation. Because the 650 nm excitation line is spectrally distant from the 493 nm collected photons, once a photon is collected there can be no further excitation events, eliminating the first mechanism for double excitations.

We now estimate the expected error from the second mechanism of double excitation errors. We evolve the optical Bloch equations for the excitation and emission in the regime where  $T_p \sim \tau_e$ , keeping track of whether the resulting  $6^2S_{1/2}$  state population comes from decays from the desired  $6^2P_{1/2}$  state ( $|e\rangle$ ). We find that favorable branching ratios and Clebsch-Gordan coefficients still

lead to high-fidelity entanglement, even though  $T_p \ll \tau_e$ , as seen in Fig. 1(b). This significantly relaxes the need for ultrafast excitation pulses, since pulse durations  $T_p \sim \tau_e = 10$  ns can be created with a CW source and standard acousto-optic (AO) or electro-optic (EO) intensity modulators. The experiments presented in this work are performed with 10 ns pulses generated by an AO modulator.

### 3. Pure single photons

Next, we wish to demonstrate the purity of our system as a single photon source to verify a low level of double excitation errors [25]. To show this, a  $^{138}\text{Ba}^+$  ion is initialized in the the  $5^2D_{3/2}(m_J = +3/2)$  stretch state by applying all polarizations of 493 nm light, and  $\sigma^+$  and  $\pi$  polarizations of 650 nm light. Next, a 10 ns pulse of  $\sigma^-$  polarized light at 650 nm excites the atom to  $|e\rangle$  (see Fig. 1(a)). We collect the resulting 493 nm fluorescence photons with an  $NA = 0.6$  objective and through a 50/50 beamsplitter with avalanche photodiode (APD) detectors behind each port as shown in Fig. 1(c). To avoid collecting light from the initialization cycle the APDs are gated closed except for a 200 ns window triggered by the 650 nm pulse. This window is much larger than the  $\sim 10$  ns lifetime of the excited state.

The normalized second-order autocorrelation function after integrating for 18 hours is plotted in Fig. 2(a). The strong suppression of the  $\tau = 0$  peak demonstrates the purity of the system as a single-photon source. In Fig. 2(b) we present  $g^{(2)}(\tau = 0)$  as a function of the fraction of light collected, which is given by the integration window. We report a value of  $g^{(2)}(0) = (8.1 \pm 2.3) \times 10^{-5}$  using a 30 ns integration window. This window includes 97% of the collected photons while keeping excessive dark counts from contaminating the signal. We measure 12 coincident events at zero delay ( $\tau = 0$ ) and a total 149,107 coincidence events for the same integration window between adjacent experiments.

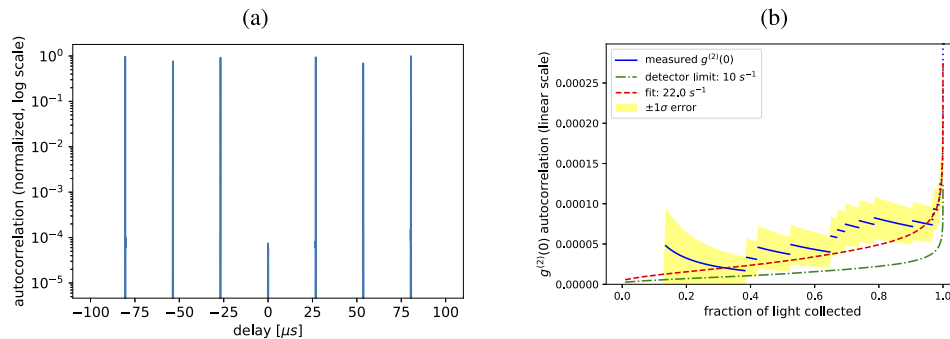


**Fig. 2.** (a) Normalized second-order autocorrelation function. 26  $\mu\text{s}$  peak spacing corresponds to experimental repetition rate. Strong suppression of  $\tau = 0$  peak demonstrates purity of single photon source. (b) Measured  $g^{(2)}(0)$  value plotted in blue against the fraction of light collected in the neighboring bright peak for the same integration time.  $1\sigma$  error bars for this data are shown in yellow. The detector dark-count limited  $g^{(2)}(0)$  is shown in green and the  $g^{(2)}(0)$  value given a fitted, constant background count rate of  $22\text{s}^{-1}$  is shown in red. The discontinuous jumps in the blue data plot correspond to coincidence detection events.

This result represents the lowest value ever recorded for a source of indistinguishable photons [22] and is consistent with the lowest value reported in any system of  $g^{(2)}(0) = (7.5 \pm 1.6) \times 10^{-5}$  [26]. Dark counts on our detectors limit  $g^{(2)}(0)$  to  $\geq 3 \times 10^{-5}$ , and we attribute the extra counts to observed transient light leakage through our AO modulators. This rate of multi-photon generation limits the contribution of the first mechanism of double excitation errors to a negligible value of  $\leq 4 \times 10^{-5}$ . Moreover, as we show below, these single photons are entangled with the atomic memory, making them useful for networking applications.

#### 4. Atomic decay polarizations

Next we examine errors in ion-photon entanglement fidelity that can result from polarization mixing. These errors can be avoided by using photonic degrees of freedom other than polarization, but as polarization qubits are easy to manipulate, they remain a popular choice [21]. There exist several different protocols for generating entanglement between an ion's spin state and the polarization of an emitted photon [27–29]. One common element is that they rely on faithfully mapping polarizations from atomic decays onto orthogonal polarization modes. When the photons are collected in a single mode fiber, the polarization modes can be made orthogonal when the fiber mode is aligned along certain axes [30,31]. But in free space, the polarization qubit begins to mix over finite solid angles of collection, leading to entanglement errors.

Consider a single atom with a quantization axis from an external magnetic field pointing in the  $z$ -direction undergoing spontaneous emission. The emitted photon can carry angular momentum of  $\Delta m_z = +1, 0,$  or  $-1$  quanta along  $z$ , and we will refer to these as  $\sigma^+$ ,  $\pi$ , and  $\sigma^-$  events respectively. For an unpolarized atom there is equal probability of emitting into each of these three modes, with spatial emission patterns given by normalized vector spherical harmonics. However, for our atoms prepared in  $|6P_{1/2}, m_J = +1/2\rangle$  as shown in Fig. 1(a) and accounting for the Clebsch-Gordan coefficients, the 493 nm emission patterns are plotted in Fig. 3(a) and are given by [28]:

$$\pi = i\sqrt{\frac{3}{16}} \sin \theta \hat{\theta}, \quad \sigma^+ = ie^{i\phi} \sqrt{\frac{3}{16}} (\cos \theta \hat{\theta} + i\hat{\phi}), \quad \sigma^- = 0 \quad (1)$$

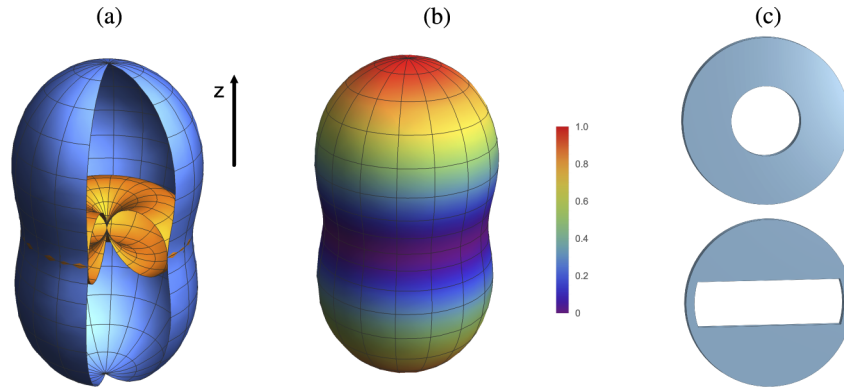


**Fig. 3.** (a) Spatial distribution of light from a  $\sigma$ -polarized (blue) and  $\pi$ -polarized (yellow) emission along the  $z$  quantization axis. Note that in the  $x$ - $y$  plane at polar angle  $\theta = \pi/2$  there are equal amounts of  $\sigma$  and  $\pi$  emission. (b) Polarization mixing from the  $\sigma$ -polarized emission pattern when measured about an axis perpendicular to the magnetic field. The color gradient shows the ratio of vertical to horizontal polarized light collected about this axis. At  $\theta = \pi/2$  there is no vertical component to the collected light. (c) Two types of apertures are analyzed in this experiment. Circular stop (top) used to restrict collection angle while maintaining a circular aperture. Horizontal stop (bottom) used to restrict collection in the  $\theta$  (vertical) direction while allowing full collection in the  $\phi$  (horizontal) direction.

After a photon is emitted and we take the projection perpendicular to the magnetic field, where the polarization bases  $(\hat{\theta}, \hat{\phi})$  project to  $(\hat{V}, \hat{H})$ , the resultant atom-photon state is given by

$$\Psi_r = \frac{1}{\sqrt{2}} \left( -e^{i\phi} |\downarrow H\rangle + ie^{i\phi} \cos \theta |\downarrow V\rangle + 0 \cdot |\uparrow H\rangle + i \sin \theta |\uparrow V\rangle \right) \quad (2)$$

When light is collected away from  $\theta = \pi/2$  this state deviates from the desired Bell state  $\Psi_d = \frac{1}{\sqrt{2}}(|\downarrow H\rangle + |\uparrow V\rangle)$ . Here, *w.l.o.g.* we have chosen the arbitrary internal phase which is controlled in experiment with waveplates, and dropped the azimuthal phase which results only in a spatial shift [32] that is unimportant for large detectors. In the limit of small solid angle, the fidelity is given by  $F = |\langle \Psi_d | \Psi_r \rangle|^2 = \frac{1}{4} (1 + \sin \theta)^2$ , and the error  $\epsilon = 1 - F$  is plotted in Fig. 3(b). The two sources of error are the unequal populations of  $\pi$  and  $\sigma^+$  emission, and the mixing of  $\sigma^+$  light with both the  $|H\rangle$  and  $|V\rangle$  atomic states. When collecting this light in free-space onto a detector as in this work, we integrate the intensity over the collection area  $\Omega$ , forming a mixed state given by  $\rho_r = \int_{\Omega} |\Psi_r\rangle \langle \Psi_r| d\Omega$ . When calculating the fidelity over this large collection area  $F = \langle \psi_d | \rho_r | \psi_d \rangle = \frac{1}{\Omega} \int_{\Omega} \frac{1}{4} (1 + \sin \theta)^2$  we find that the biggest source of error is the population mixed into  $|\downarrow V\rangle$ . The fidelity is plotted as a function of solid angle collected in the blue curve of Fig. 4(a). This result confirms that as larger solid angles are used to improve entanglement generation rates, the fidelity of free-space ion-photon entanglement will suffer.

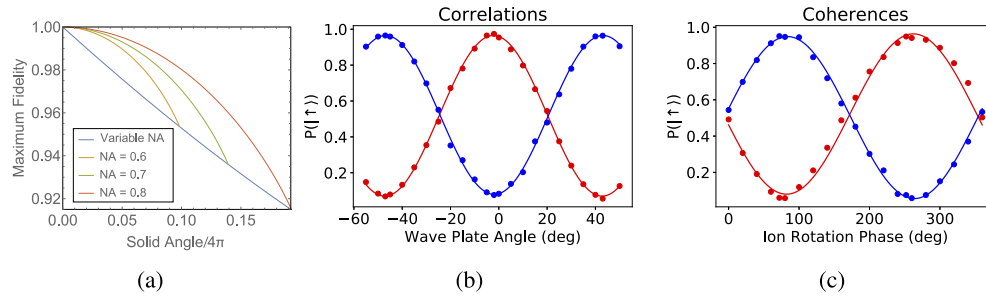


**Fig. 4.** (a) Theoretical scaling between solid angle of light collection and polarization-mixing errors on ion-photon fidelity. The blue curve represents the scaling for a simple circular aperture. The yellow, green, and red curves give the scaling assuming a fixed circular aperture of NA = 0.6, 0.7, or 0.8 respectively with added horizontal apertures that restrict collection in the  $\theta$  direction. (b) Ion-photon correlation results as a function of wave plate rotation angle. The red (blue) curve shows the probability of finding the ion in the  $|\uparrow\rangle$  state when the photon is detected on APD1 (APD2). No stops were used for these experiments. (c) Coherences in the y-basis are taken by setting the half-wave plate to perform a  $\pi/2$  rotation on the photon and then applying a  $\pi/2$  pulse on the ion with a varying phase.

To experimentally examine this polarization mixing, we perform ion-photon entanglement using a single trapped  $^{138}\text{Ba}^+$  atom. First, we use 650 nm excitation to generate an entangled ion-photon pair as described in previous sections. For this experiment, we also make use of the half-wave plate that can rotate the photon's polarization before the polarization measurement. Additionally, ion spin state rotations and readout are performed using the methods described in [18].

To demonstrate entanglement, we first directly show correlations between the state of the ion and the photon by analyzing these correlations as a function of photon rotation angle. Next, the coherences are measured by fixing the wave plate angle to rotate the polarization by  $\pi/2$  and performing a  $\pi/2$  Raman rotation on the atom with a variable phase. These results are plotted in Fig. 4 and show an ion-photon entanglement fidelity of  $F = 0.884(4)$  when light is collected over the entire circular 0.6 NA of the lens. Intrinsic polarization mixing for this size of aperture accounts for a fidelity loss of 0.046; we attribute the remaining errors to imperfect state initialization and readout, intensity and phase noise on the Raman beams used to analyze the coherences, and polarization mixing in the collection optics [19]. The analysis from previous sections indicates that errors from double excitations contribute an error of  $<0.004$ .

To analyze the effects of spatial filtering on ion light, various optical stops were inserted immediately after the microscope objective (see Fig. 3(c)). These apertures were designed to block just over half of the solid angle either symmetrically (circular stops) or in only the  $\theta$  direction (horizontal stops). After inserting the stops, the entanglement experiments were repeated; the circular stops gave a fidelity of 0.912(5) and the horizontal stops improved this further to 0.930(4). These results are shown along with the theory curves in Table 1 and confirm that, by taking into consideration the spatial profile of the atomic fluorescence, we can maximize fidelity gained by sacrificing rate.

**Table 1. Here we compare our experimental results using the various apertures with the expected results from the theoretical curves presented in Fig. 4 scaled to account for other sources of error in the system. Our results are highly consistent with a favorable trade-off of collection rate and fidelity from the use of horizontal apertures.**

Aperture Type	Solid Angle/ $4\pi$	Expected Fidelity	Measured Fidelity
Circular	0.100	0.887	0.884(4)
Circular	0.050	0.912	0.912(5)
Horizontal	0.050	0.927	0.930(3)

For future quantum networks, the pure entangled photons demonstrated in this work can be combined with techniques for performing local operations described in previous works [18] to construct a modular node consisting of a superior Yb memory qubit and visible photon flying qubits. This Yb memory is unaffected by the photon generation process, allowing for local operations or storage while the Ba-photon link is created. Multiple nodes can be connected together using a photonic Bell state analyzer [10,33] to create a distributed network for quantum information processing [34].

## Funding

National Science Foundation (EFMA-1741651, PFCQC 17-548, PHY0822671); Intelligence Advanced Research Projects Activity (IARPA-BAA-15-10); Army Research Office (ONR-15-FOA-0011); Air Force Office of Scientific Research (ONRBAA12-020); Army Research Laboratory (AFRL-AFOSR-2016-0007, W911NF-12-R-0011-02).

## Acknowledgments

We acknowledge the useful discussions with D. Nadlinger and D. Lucas.

## Disclosures

The authors declare that there are no conflicts of interest related to this article.

## References

1. J. I. Cirac, P. Zoller, H. J. Kimble, and H. Mabuchi, "Quantum state transfer and entanglement distribution among distant nodes in a quantum network," *Phys. Rev. Lett.* **78**(16), 3221–3224 (1997).
2. S. Wehner, D. Elkouss, and R. Hanson, "Quantum internet: A vision for the road ahead," *Science* **362**(6412), eaam9288 (2018).
3. H. J. Kimble, "The quantum internet," *Nature* **453**(7198), 1023–1030 (2008).
4. N. Sangouard, R. Dubessy, and C. Simon, "Quantum repeaters based on single trapped ions," *Phys. Rev. A* **79**(4), 042340 (2009).
5. S. Ritter, C. Nölleke, C. Hahn, A. Reiserer, A. Neuzner, M. Uphoff, M. Mücke, E. Figueroa, J. Bochmann, and G. Rempe, "An elementary quantum network of single atoms in optical cavities," *Nature* **484**(7393), 195–200 (2012).
6. A. Reiserer and G. Rempe, "Cavity-based quantum networks with single atoms and optical photons," *Rev. Mod. Phys.* **87**(4), 1379–1418 (2015).
7. J. I. Cirac and P. Zoller, "Quantum computations with cold trapped ions," *Phys. Rev. Lett.* **74**(20), 4091–4094 (1995).

8. K. Mølmer and A. Sørensen, "Multiparticle entanglement of hot trapped ions," *Phys. Rev. Lett.* **82**(9), 1835–1838 (1999).
9. L. Duan, B. B. Blinov, D. L. Moehring, and C. R. Monroe, "Scalable trapped ion quantum computation with a probabilistic ion-photon mapping," *Quantum Inf. & Comput.* **4**, 165–173 (2004).
10. P. Maunz, D. L. Moehring, S. Olmschenk, K. C. Younge, D. N. Matsukevich, and C. Monroe, "Quantum interference of photon pairs from two remote trapped atomic ions," *Nat. Phys.* **3**(8), 538–541 (2007).
11. B. B. Blinov, D. L. Moehring, L.-M. Duan, and C. Monroe, "Observation of entanglement between a single trapped atom and a single photon," *Nature* **428**(6979), 153–157 (2004).
12. T. Sauter, W. Neuhauser, R. Blatt, and P. E. Toschek, "Observation of quantum jumps," *Phys. Rev. Lett.* **57**(14), 1696–1698 (1986).
13. G. Aranedá, D. B. Higginbottom, L. Slodicka, Y. Colombe, and R. Blatt, "Interference of single photons emitted by entangled atoms in free space," *Phys. Rev. Lett.* **120**(19), 193603 (2018).
14. R. D. Graham, S.-P. Chen, T. Sakrejda, J. Wright, Z. Zhou, and B. B. Blinov, "A system for trapping barium ions in a microfabricated surface trap," *AIP Adv.* **4**(5), 057124 (2014).
15. D. Yum, D. D. Munshi, T. Dutta, and M. Mukherjee, "Optical barium ion qubit," *J. Opt. Soc. Am. B* **34**(8), 1632–1636 (2017).
16. D. Hucul, J. E. Christensen, E. R. Hudson, and W. C. Campbell, "Spectroscopy of a synthetic trapped ion qubit," *Phys. Rev. Lett.* **119**(10), 100501 (2017).
17. J. D. Siverns, X. Li, and Q. Quraishi, "Ion-photon entanglement and quantum frequency conversion with trapped Ba<sup>+</sup> ions," *Appl. Opt.* **56**(3), B222–B230 (2017).
18. I. V. Inlek, C. Crocker, M. Lichtman, K. Sosnova, and C. Monroe, "Multispecies trapped-ion node for quantum networking," *Phys. Rev. Lett.* **118**(25), 250502 (2017).
19. D. Hucul, I. V. Inlek, G. Vittorini, C. Crocker, S. Debnath, S. M. Clark, and C. Monroe, "Modular entanglement of atomic qubits using photons and phonons," *Nat. Phys.* **11**(1), 37–42 (2015).
20. L. Slodička, G. Hétet, N. Röck, P. Schindler, M. Hennrich, and R. Blatt, "Atom-atom entanglement by single-photon detection," *Phys. Rev. Lett.* **110**(8), 083603 (2013).
21. D. L. Moehring, P. Maunz, S. Olmschenk, K. C. Younge, D. N. Matsukevich, L.-M. Duan, and C. Monroe, "Entanglement of single-atom quantum bits at a distance," *Nature* **449**(7158), 68–71 (2007).
22. D. B. Higginbottom, L. Slodicka, G. Aranedá, L. Lachman, R. Filip, M. Hennrich, and R. Blatt, "Pure single photons from a trapped atom source," *New J. Phys.* **18**(9), 093038 (2016).
23. M. Bock, P. Eich, S. Kucera, M. Kreis, A. Lenhard, C. Becher, and J. Eschner, "High-fidelity entanglement between a trapped ion and a telecom photon via quantum frequency conversion," *Nat. Commun.* **9**(1), 1998 (2018).
24. N. Yu, W. Nagourney, and H. Dehmelt, "Radiative lifetime measurement of the Ba<sup>+</sup> metastable D<sub>3/2</sub> state," *Phys. Rev. Lett.* **78**(26), 4898–4901 (1997).
25. M. Mücke, J. Bochmann, C. Hahn, A. Neuzner, C. Nölleke, A. Reiserer, G. Rempe, and S. Ritter, "Generation of single photons from an atom-cavity system," *Phys. Rev. A* **87**(6), 063805 (2013).
26. L. Schweickert, K. D. Jons, K. D. Zeuner, S. F. Covre da Silva, H. Huang, T. Lettner, M. Reindl, J. Zichi, R. Trotta, A. Rastelli, and V. Zwiller, "On-demand generation of background-free single photons from a solid-state source," *Appl. Phys. Lett.* **112**(9), 093106 (2018).
27. C. Simon and W. T. M. Irvine, "Robust long-distance entanglement and a loophole-free bell test with ions and photons," *Phys. Rev. Lett.* **91**(11), 110405 (2003).
28. L. Luo, D. Hayes, T. Manning, D. Matsukevich, P. Maunz, S. Olmschenk, J. Sterk, and C. Monroe, "Protocols and techniques for a scalable atom-photon quantum network," *Fortschr. Phys.* **57**(11-12), 1133–1152 (2009).
29. T. E. Northup and R. Blatt, "Quantum information transfer using photons," *Nat. Photonics* **8**(5), 356–363 (2014). Review Article.
30. T. Kim, P. Maunz, and J. Kim, "Efficient collection of single photons emitted from a trapped ion into a single-mode fiber for scalable quantum-information processing," *Phys. Rev. A* **84**(6), 063423 (2011).
31. D. Nadlinger and D. Lucas, (private communication).
32. G. Aranedá, S. Walser, Y. Colombe, D. B. Higginbottom, J. Volz, R. Blatt, and A. Rauschenbeutel, "Wavelength-scale errors in optical localization due to spin-orbit coupling of light," *Nat. Phys.* **15**(1), 17–21 (2019).
33. C. Nölleke, A. Neuzner, A. Reiserer, C. Hahn, G. Rempe, and S. Ritter, "Efficient teleportation between remote single-atom quantum memories," *Phys. Rev. Lett.* **110**(14), 140403 (2013).
34. C. Monroe, R. Raussendorf, A. Ruthven, K. R. Brown, P. Maunz, L.-M. Duan, and J. Kim, "Large-scale modular quantum-computer architecture with atomic memory and photonic interconnects," *Phys. Rev. A* **89**(2), 022317 (2014).